1 Combined use of Mie-Raman and fluorescence lidar observations for improving aerosol

2 characterization: feasibility experiment

3

4 Igor Veselovskii[1], Qiaoyun Hu[2], Philippe Goloub[2], Thierry Podvin[2], Mikhail Korenskiy[1], Olivier

5 Pujol[2], Oleg Dubovik[2], Anton Lopatin[3]

6 *[1]Prokhorov General Physics Institute of the Russian Academy of Sciences, Moscow, Russia.*

7 *[2]Univ. Lille, CNRS, UMR 8518 - LOA - Laboratoire d'Optique Atmosphérique, Lille F-59000,*

8 *France*

9 *[3]GRASP-SAS, Villeneuve d'Ascq, France*

10

11 Abstract

12 To study the feasibility of a fluorescence lidar for aerosol characterization, the fluorescence

13 channel is added to LILAS - multiwavelength Mie-Raman lidar of Lille University, France. A

14 part of fluorescence spectrum induced by 355 nm laser radiation, is selected by the interference

15 filter of 44 nm bandwidth centered at 466 nm. Such an approach has proved high sensitivity,

16 allowing to detect fluorescence signals from weak aerosol layers and to calculate the

17 fluorescence backscattering coefficient from the ratio of fluorescence and nitrogen Raman

18 backscatters. Observations were performed during November 2019 – February 2020 period. The

19 fluorescence capacity (ratio of fluorescence to elastic backscattering coefficients), measured at

20 the condition of low relative humidity, varied in a wide range, being the highest for the smoke

21 and the lowest for the dust particles. The results presented demonstrate also, that the

22 fluorescence measurements can be used for monitoring the aerosol inside the cloud layers.

23

24 1. Introduction

25   The aerosol – cloud interaction is one of the key factors influencing the Earth radiation

26 balance and, for its realistic modeling, knowledge of aerosol properties both outside and within

27 the cloud layer are needed. The multiwavelength Mie-Raman and HSRL lidars, measuring

28 aerosol backscattering and extinction coefficients at multiple wavelengths, are widely used for

29 remote characterization of aerosol properties (e.g. Tesche et al., 2011; Burton et al., 2012, Luís

30 Guerrero-Rascado et al., 2018; Veselovskii et al., 2020 and references therein). However,

31 although useful for studying aerosol, the amount of information contained in these measurements

32 remains limited (Burton et al., 2016; Alexandrov and Mishchenko, 2017). In addition, such lidars

33 are not able to detect and characterize aerosol inside a cloud layer, because aerosol scattering is

34 masked by the strong cloud particles scattering. To improve the lidar capability for aerosol

35 characterization, additional channels, measuring the laser induced fluorescence, can be used.

36 Fluorescence spectroscopy is a highly sensitive technique, widely used for the in-situ monitoring
37 of atmospheric organic particles (Pan et al., 2007, 2015; Miyakawa et al., 2015; Huffman et al.,
38 2019). The synergy of fluorimetry and lidar technology provides an opportunity to perform such
39 monitoring remotely (Immler et al., 2005; Rao et al., 2018; Saito et al., 2018). Numerous types
40 of atmospheric aerosols, such as biological, biomass burning particles, sulfates and even dust are
41 fluorescent, being excited by UV radiation. When the excitation wavelength is 355 nm, the main
42 part of emission spectra is usually contained within the 400–650 nm range (Pan et al., 2015). The
43 fluorescence spectrum varies with the aerosol types/composition, making therefore possible their
44 identification. Moreover, due to the fact that pure water does not fluoresce, the measurement of
45 cloud fluorescence allows to get information about aerosol particles within cloud layer, at least
46 near the cloud base, thus allowing to investigate the aerosol – cloud coexistence.

47   One of the factors that intricate obtaining the quantitative information about aerosol
48 properties from fluorescence measurements, is influence of the relative humidity (RH). The
49 aerosol particles grow by water uptake, changing their elastic scatter cross-section, but the
50 change in water percentage within an aerosol particle, normally does not alter the chemical
51 components, so total amount of fluorescent molecules within a particle does not change.
52 However the illumination intensity distribution within a particle, as well as the emission angle
53 distribution will be altered by the change of particle size, shape and refractive index, and this
54 modification may affect the fluorescence measurement. The phase functions of the microspheres
55 for the incoherent scattering (fluorescence is an example of incoherent scattering), were
56 computed in works of Kerker and Druger (1979) and Veselovskii et al. (2002a). Results
57 demonstrate, that fluorescence of particles dissolved in water microspheres can be increased in
58 the backward direction by factor ~2, comparing to fluorescence of a bulk material (calculated per
59 gram of solid matter). This enhancement, however, occurs for relatively big microspheres with
60 size parameter $x = \dfrac{2\pi r}{\lambda}$ exceeding approximately 10 (Veselovskii et al., 2002a). For the
61 wavelength λ=532 nm corresponding radius r is about 1.0 μm, so fluorescence of the fine mode
62 particles should be affected less by the hygroscopic growth. We should mention also that for
63 insoluble particles, the presence of the water shell, at the condition of high RH, in principle, can
64 lead to an additional increase of the fluorescence, due to the water droplet lens effect. Similar
65 effect is well known for the soot particles covered by non-absorbing shell (Schnaiter, 2005).

66   Interpretation of fluorescent measurements in a cloud is even more challenging. The
67 liquid cloud is a mixture of interstitial aerosol particles (non-activated particles) and droplets,
68 formed on the cloud condensation nucleus (CCNs). The CCNs may be completely dissolved in
69 the droplet, or survived as a solid particle within the droplet, as is the case for dust or soot. The

70 relative contributions of interstitial aerosol and activated CCNs in the droplets to the total cloud

71 fluorescence backscatter are unknown, and the need to estimate these contributions was one of

72 the motivations of this study.

73   The recent interest in fluorescence lidars was stimulated also by the progress in the

74 development of the multianode photomultipliers allowing, in combination with spectrometer,

75 simultaneous detection of lidar signal in 32 spectral bins (Sugimoto et al., 2012; Reichardt et al.,

76 2014, 2017; Saito et al., 2018). Such multichannel detection has the obvious advantage to

77 analyze the whole spectrum, allowing the aerosol identification. However, sensitivity of such

78 lidar spectrometers is lower when compared to the technique based on selection of fluorescence

79 spectrum intervals with interference filters, because the transmission of modern filters exceeds

80 90%. The use of interference filters, in addition to being more sensitive, allows more affordable

81 modification of a multiwavelength Mie-Raman lidar by adding one or more fluorescence

82 channels. To obtain the highest sensitivity, it is mandatory to acquire the fluorescence in a wide

83 spectral range which, however, makes the data analysis more complicated, because variation of

84 aerosol and molecular transmission within the detection spectral range has to be accounted for.

85 In addition, in Mie-Raman multi-wavelength lidars one should avoid the spectral intervals

86 affected by elastic scattering and corresponding strong Raman lines.

87   In our paper we present the results of a feasibility experiment and evaluate the sensitivity

88 of a single-channel fluorescence lidar. Measurements were performed at *Laboratoire d'Optique*

89 *Atmosphérique* (LOA) during November 2019 – February 2020 period. During that period, the

90 aerosol load was very low, so we were not able to determine the particle properties from

91 multiwavelength observations. The objective was then to estimate the efficiency /added value of

92 the fluorescence channel. We therefore mainly focus on analysis of efficiency of fluorescence

93 lidar monitoring of different types of aerosol and on detection of aerosol particles inside low

94 level cloud layers.

95

96 **2. Experimental setup and data analysis**

97   The measurements were performed using the LILAS - multiwavelength Mie-Raman

98 lidar, based on a tripled Nd:YAG laser with a 20 Hz repetition rate and pulse energy of 70 mJ at

99 355 nm. The backscattered light is collected by a 40 cm aperture Newtonian telescope. The

100 system is designed for simultaneous detection of elastic and Raman backscatters, allowing the so

101 called $3\beta+2\alpha+3\delta$ data configuration, including three particle backscattering (β), two extinction

102 (α) coefficients along with three depolarization ratios (δ). Description of the system can be found

103 in recent publication of Hu et al., 2019. The aerosol extinction and backscattering coefficients at

104 355 and 532 nm were calculated from Mie-Raman observations (Ansmann et al., 1992) while

105 backscattering at 1064 nm was derived by the Klett method (Klett, 1985).

106   For the experiment described, the system was modified: water vapor 408 nm Raman filter

107 was replaced by a fluorescence one. Corresponding optical scheme together with transmission

108 curve of the interference filter in the fluorescence channel are shown in Fig.1. The nitrogen

109 Raman and fluorescence optical signals are separated by a dichroic mirror: more than 98% of

110 387 nm radiation is reflected and more than 95% of fluorescence signal is transmitted. For both

111 nitrogen Raman and fluorescence channels, the R9880U-01 PMTs were used. A part of the

112 wideband fluorescence signal was selected by an Alluxa interference filter centered at 466 nm

113 with 44 nm bandwidth. The filter transmission, at maximum, exceeds 98%. The operational band

114 was chosen outside of the overtones of O_2 and N_2 vibrational Raman lines. In addition, the

115 transmission of the selected fluorescence filter band matches the maxima of fluorescence of

116 many organic molecules (Saito et al., 2018; Reichardt et al., 2017). Filter provides OD6

117 suppression outside the transmission band. To increase the suppression, two identical

118 interference filters were used in tandem. For additional rejection of elastic scattering at 355 nm

119 and 532 nm the two-band notch filter was used. With such design, we estimate that the total

120 suppression of elastic scattering in the fluorescence channel is above OD14. In this paper,

121 observations were carried out during night-time only.

122   In an elastic channel, the backscattered radiative power P_L, at distance z is described by

123 the lidar equation

124 $$P_L = O(z)\frac{1}{z^2}C_L(\beta_L^a + \beta_L^m)\exp\left\{-2\int_0^z (\alpha_L^a + \alpha_L^m)dz'\right\} = O(z)\frac{1}{z^2}C_L(\beta_L^a + \beta_L^m)T_L^2 \qquad (1)$$

125 Here $O(z)$ is the geometrical overlap factor, which is assumed to be the same for elastic, Raman

126 and fluorescence channels. C_L is the range independent constant, including efficiency of

127 detection channel. T_L is one-way transmission, describing light losses on the way from the lidar

128 to distance z at laser wavelength λ_L. Backscattering and extinction coefficients contain aerosol

129 and molecular contributions: $\beta_L^a + \beta_L^m$ and $\alpha_L^a + \alpha_L^m$, where the superscripts "a" and "m" indicate

130 aerosol and molecular scattering, respectively.

131   In a Raman channel, the backscatter radiative power, P_R , can be rewritten as:

132 $$P_R = O(z)\frac{1}{z^2}C_R\beta_R\exp\left\{-\int_0^z (\alpha_L^a + \alpha_R^a + \alpha_L^m + \alpha_R^m)dz'\right\} = O(z)\frac{1}{z^2}C_R\beta_R T_L T_R \qquad (2)$$

133 Here T_R is the atmospheric transmission at Raman wavelength λ_R. Raman backscattering

134 coefficient is:

135     $\beta_R = N_R \sigma_R ,$ (3)

136   where N_R is the number of Raman scatters (per unit of volume) and σ_R is the Raman differential

137   scattering cross section in the backward direction. To account for spectral dependence of aerosol

138   extinction, the Angstrom exponent γ is used:

139     $\dfrac{\alpha_L^a}{\alpha_R^a} = \left(\dfrac{\lambda_R}{\lambda_L} \right)^{\gamma}$ (4)

140   The aerosol backscattering and extinction coefficients can be computed from Mie – Raman lidar

141   observations using equations (1-4), as shown by Ansmann et al. (1992).

142   In the case of the fluorescence, the emitted wavelengths are spread over wide spectral

143   range, so the spectral dependence of aerosol and molecular extinction coefficients, inside the

144   fluorescence band, should be considered. Moreover, the spectral differential fluorescence cross

145   section $\dfrac{d\sigma_F}{d\lambda}(\lambda, r)$ depends on particle size (Hill, et al., 2015), so the particle size distribution

146     $\dfrac{dN(r)}{dr}$, which is the number of particles with radii between r and $r+dr$ per unit of volume, has

147   to be considered. The radiative power in the fluorescence channel within the spectral interval

148     $[\lambda_{min}, \lambda_{max}]$ is:

149     $P_F = O(z) \dfrac{1}{z^2} T_L \int\limits_{\lambda_{min}}^{\lambda_{max}} \int\limits_{r_{min}}^{r_{max}} C_F(\lambda) \times \dfrac{dN(r)}{dr} \times \dfrac{d\sigma_F}{d\lambda}(\lambda, r) \times \exp\left\{ -\int\limits_0^z [\alpha^a(\lambda, z') + \alpha^m(\lambda, z')]dz' \right\} drd\lambda$ (5)

150   The spectral dependence of $C_F(\lambda)$ is determined mainly by the transmission of the interference

151   filter in the fluorescence channel. If the filter spectral width $\lambda_{max} - \lambda_{min}$ is not very high, the

152   procedure of data analysis can be simplified. The atmospheric transmission for fluorescence

153   signal

154     $T_F(\lambda) = \exp\left\{ -\int\limits_0^z [\alpha^a(\lambda, z') + \alpha^m(\lambda, z')]dz' \right\}$ (6)

155   can be taken at wavelength λ_F, corresponding to the center of the filter transmission band

156     $T_F(\lambda) = T_F(\lambda_F) \equiv T_F$. The filter transmission used (Fig.1) is close to rectangular and sensitivity

157   of the PMT used doesn't vary significantly within $[\lambda_{min}, \lambda_{max}]$ interval, which means the

158   calibration constant C_F can be considered as spectrally independent. Expression (5) can be

159   rewritten, by introducing the fluorescence backscattering coefficient β_F:

160     $\int\limits_{\lambda_{min}}^{\lambda_{max}} \int\limits_{r_{min}}^{r_{max}} \dfrac{dN(r)}{dr} \times \dfrac{d\sigma_F}{d\lambda}(\lambda, r) drd\lambda = \int\limits_{r_{min}}^{r_{max}} \dfrac{dN(r)}{dr} \times \sigma_F(r) dr = \beta_F$ (7)

161   Here $\sigma_F(r) = \int_{\lambda_{\min}}^{\lambda_{\max}} \dfrac{d\sigma_F}{d\lambda}(\lambda,r)d\lambda$ is the effective fluorescence differential cross section, integrated

162   over spectral interval $[\lambda_{\min}, \lambda_{\max}]$. The use of β_F allows to rewrite equation (5) for the power of

163   the fluorescence backscattering similarly to the Raman one.

164      $$P_F = O(z)\frac{1}{z^2}C_F\beta_F T_F T_L \tag{8}$$

165   The fluorescence backscattering coefficient, β_F, can be obtained from the ratio of

166   equations (8) and (2) for fluorescence and Raman backscatters:

167      $$\beta_F = \frac{C_R}{C_F}\frac{P_F}{P_R}N_R\sigma_R\frac{T_R}{T_F} \tag{9}$$

168   The ratio of atmospheric transmissions at λ_R and λ_F wavelengths (T_R/T_F) can be calculated the

169   same way as for water vapor measurements (Ansmann et al., 1992; Whiteman et al., 2006). In

170   our study, for the nitrogen molecule we used Raman scattering cross section at 355 nm

171      $\sigma_R = 2.1 * 10^{-30}$ cm^2 (Burris et al., 1992), but, to obtain absolute values of β_F, C_R/C_F ratio must be

172   determined. This ratio can be found from calibration, performed by using a lamp with known

173   spectrum, as it has been done for the Raman water vapor lidars (Venable et al., 2011), but at

174   current stage, we use simplified approach for estimation of C_R/C_F. The dichroic optics used,

175   allows efficient separation of fluorescence and Raman signals, so main source of uncertainty is

176   relative sensitivity of PMTs in the channels. To equalize sensitivities, the PMT from

177   fluorescence channel was installed in the Raman one and by small adjusting of voltage the same

178   value of nitrogen Raman signal was obtained. The cathode sensitivity of R9880U-01 PMT

179   between 387 nm and 466 nm changes for less than 15%, thus we assume that sensitivities of

180   PMTs in both channels are the same and only difference in transmission of interference filters

181   was considered. In all results presented below $C_R/C_F = 0.7$ value was used.

182   To characterize the efficiency of the fluorescence respect to elastic scattering, it is

183   convenient to consider also the particle fluorescence capacity,

184      $$G_F = \frac{\beta_F}{\beta_L}, \tag{10}$$

185   which is the ratio of fluorescence and aerosol elastic backscattering coefficients (Reichardt et al.,

186   2017). Here and below, for simplicity, we will use notation $\beta^a \equiv \beta$. The aerosol loading in the

187   atmosphere during the experiment was very low and, in order to decrease the interference of the

188   Raleigh scattering, the backscatter at 1064 nm was mainly used for aerosol characterization,

189   while for the cloud layers the backscattering coefficients at 355 and 532 nm were used as well.

190   Multiwavelengtn Mie-Raman lidar measurements allow estimation of the particle number

191 density $N = \int\limits_{r_{\min}}^{r_{\max}} \dfrac{dN(r)}{dr} dr$ as well as their total volume V (Müller et al., 1999; Veselovskii et al.,

192 2002b), thus a mean fluorescence cross section per a single particle can be estimated as

193 $\sigma_F^N = \dfrac{\beta_F}{N}$. Assuming, that in the simplest case, a fluorescence backscattering coefficient is

194 proportional to the particle volume, we can estimate the fluorescence cross section per a unit

195 particle volume as $\sigma_F^V = \dfrac{\beta_F}{V}$. Thus, synergy of Mie-Raman and fluorescence lidar measurements

196 should allow remote characterization of the particle fluorescent properties. We should mention

197 however, that estimation of σ_F^V makes sense only at low RH, because water uptake by the

198 particle will alter results.

199

200 **3. Observation results.**

201   *3.1. Fluorescence of aerosol layers.*

202   The measurements reported were performed during November 2019 – February 2020

203 period at the Lille Atmospheric Observation Platform (https://www-loa.univ-

204 lille1.fr/observations/plateformes.html?p=apropos) hosted by Laboratoire d'Optique

205 Atmospherique, University of Lille, Hauts-de-France region. Two examples of measurement are

206 presented in Fig.2 and are showing height–temporal distributions of the range corrected lidar

207 signal (RCLS) at 1064 nm, of volume depolarization ratio (δ_{1064}), and of fluorescence

208 backscattering coefficient (β_F), for the nights 29-30th November 2019 and 6-7th February 2020.

209   During the first night (left column in Fig. 2), aerosol layer is localized mainly below 2000

210 m. Though the aerosol loading is low above 2000 m ($\beta_{1064}<0.01$ Mm^{-1}sr^{-1}), it is well revealed by

211 the enhanced depolarization ratio and the enhanced fluorescence backscattering coefficient.

212 During the second night of observation (right column in Fig.2), a detached/isolated layer is

213 observed at approximately 3000 m. This layer is characterized by high depolarization ratio (the

214 particle depolarization ratio at 1064 nm in the center of the layer exceeds 15%), indicating to the

215 presence of dust. An explanation of the observed increase of fluorescence signal could be mixing

216 of mineral dust particles with organic materials (Sugimoto et al., 2012; Miyakawa et al., 2015)

217 and local aerosol during transportation.

218   The time averaged profiles (β_{1064}, β_F, G_F) for these two nights, as well as for 16th January

219 episode are shown in Fig.3. Backscattering coefficient β_{1064} was calculated by Klett method,

220 assuming a lidar ratio $S=50$ sr. Due to low aerosol extinction value, the results are not sensitive

221 to the choice of S. The HYSPLIT back trajectory analysis (Stein et al., 2015) demonstrates that

222 on 30 November and 16 January the air masses, at 3500 and 5000 m height respectively, were

223 transported from Canada, so could contain the biomass burning particles. While on 6-7 February

224 the air masses at 3000 m arrived from South – West passing near Africa, thus containing the dust

225 particles. The closest available radiosonde data are from the Herstmonceux (UK) and Ebbe

226 (Belgium) stations, located 150 km and 95 km away from the observation site respectively. Data

227 from both stations show that on the night 29-30 November 2019 the relative humidity (RH) was

228 about 70% at 1000 m and dropped below 20% above 2000 m. The fine mode of the particle size

229 distribution over the observation site is normally predominant inside the planetary boundary

230 layer (PBL). Pure water is not fluorescing, so the water uptake by the fine particles, at the

231 condition of high RH, is expected to yield an increase of elastic scattering without significant

232 effect on the fluorescence emission. The aerosol backscattering β_{1064} on 29-30th November

233 (Fig.3a) is 0.4 $Mm^{-1}sr^{-1}$ at 1000 m and decreases by a factor 40 at 1900 m, while β_F within this

234 height range changes less than twice. This is supporting the assumption that the observed

235 variation of aerosol backscattering in the PBL is mainly due to the change of the particle water

236 fraction. The water uptake at low altitudes agrees with low values of the observed particle

237 depolarization ratio δ_{1064}^p, which is below 0.5% at 1000 m. Within weak aerosol layer at the

238 range 2500 – 4000 m, the particle depolarization δ_{1064}^p is about 5% and we observe the increase of

239 fluorescence capacity G_F, with respect to the layer below 2000 m, up to $2.5*10^{-4}$. This increase

240 of G_F in the 2500 – 4000 m layer can be due to the presence of another particles type, for

241 example, biomass burning. From this episode, one can conclude that fluorescence backscattering,

242 though being almost 4 orders lower than elastic one, can be reliably detected with our current

243 lidar configuration.

244   On January 16th (Fig.3b), atmospheric RH also decreases with height, from about 80% at

245 1000 m to less than 20% above 2000 m, leading to an increase of G_F for more than one order of

246 magnitude. Such variation of G_F within the PBL is probably also related to the particle water

247 uptake, just like in Fig.3a. Aerosol backscattering increases above 3000 m and reaches its

248 maximum value at 5000 m. Within 3000 m – 5500 m range, fluorescence capacity was about

249 $2.5*10^{-4}$, which is higher than in the PBL.

250   On February 6-7th the aerosol loading in the PBL is very low (β_{1064}<0.003 $Mm^{-1}sr^{-1}$ at 1000

251 m) and RH from radiosonde at Herstmonceux is below 40% in the height range considered. At

252 3000 m, a dust layer is observed (Fig.3c). In the middle of this layer, fluorescence capacity is

253 about $0.6*10^{-4}$ which is about factor 4 lower than in the elevated layers in Fig.3a,b. Still,

254 significant value of G_F can indicate the presence of organic materials in the dust layer (Sugimoto

255 et al., 2012).

256   As discussed in section 2, lidar measurements provide an opportunity to estimate the

257 particle fluorescence cross section. For this, we need to know the particle number N and volume

258 V density in the aerosol layer, which, in principle, can be determined from the multiwavelength

259 lidar observations (Muller et al., 1999; Veselovskii et al., 2002b). In our case, however, due to

260 very low aerosol loading the extinction coefficients could not be determined. Still, the rough

261 estimations of the particle parameters can be done using the predefined aerosol model driven by

262 only a few parameters. In our study we use a simplified approach, modeling aerosol as an

263 external mixture of several aerosol components with predetermined properties. The definition of

264 aerosol components is based on global multiyear AERONET observations (Dubovik et al., 2002)

265 with some modifications. All aerosol types are described by a bimodal particle size distribution

266 (PSD)

267
$$\frac{dV}{d\ln r} = \sum_{i=f,c} \frac{C_{V,i}}{\sqrt{2\pi}\sigma_i} \exp\left[-\frac{(\ln r - \ln r_{V,i})^2}{2\sigma_i^2} \right] \tag{11}$$

268 where $C_{V,i}$ denotes the particle volume concentration, $r_{V,i}$ is the median radius, and σ_i is the

269 standard deviation. Subscripts f and c correspond to the fine and coarse mode respectively. The

270 parameters of the number size distribution $\frac{dN}{d\ln r}$ can be obtained from (11) using the

271 expressions from Horvath et al. (1990).   Table 1 shows the model parameters for three aerosol

272 types: biomass burning (BB), urban (UR) and dust (DU). From this model, the aerosol

273 backscattering and extinction coefficients can be calculated at any wavelength. As mentioned

274 above, due to low aerosol loading, we use only backscattering coefficient at 1064 nm, so Table 1

275 presents $\beta_{1064}^{N=1} = \dfrac{\beta_{1064}}{\displaystyle\int_{r_{\min}}^{r_{\max}} \dfrac{dN(r)}{dr} dr}$ - mean backscattering coefficient for a single particle ($N=1$),

276 together with corresponding complex refractive index (CRI) used in computations. Calculations

277 were performed in assumptions of spherical particles for BB and UR and for the randomly

278 oriented spheroids for dust (Dubovik, et al., 2006). The volume $V^{N=1}$ in the Table 1 is also given

279 for $N=1$ (so can be considered as a single particle average volume). Thus, if the aerosol type is

280 known, comparing of computed $\beta_{1064}^{N=1}$ from Table 1 with observed values β_{1064}, yields the

281 number and volume particle densities as $N = \dfrac{\beta_{1064}}{\beta_{1064}^{N=1}}$ and $V = N \times V^{N=1}$.

9

282   Table 2 summarizes for the three nights from Fig.3, the fluorescence cross sections per a

283 single particle, $\sigma_F^N = \dfrac{\beta_F}{N}$, and per unit volume, $\sigma_F^V = \dfrac{\beta_F}{V}$. Values are provided for the altitudes

284 corresponding to the maximum of fluorescence backscattering β_F in elevated layers, where the

285 relative humidity (RH) should be low and hygroscopic effect reduced. Basing on the back

286 trajectory analysis, particles are assumed to be of biomass burning origin for November 30th and

287 January 16th, and of dust origin for February 6-7th. We should remind, however, that our

288 estimations of N (and so σ_F^N) depend on the assumed aerosol type. The particle volume, V, is

289 however a more reliable parameter. For example, if the UR aerosol type is considered, rather

290 than the BB one, the particle number density, N, for November 30th becomes $N=21 \text{cm}^{-3}$ (instead

291 63 cm^{-3} for BB) while the total volume remains rather constant ($V=0.34$ μm$^3 \cdot$cm^{-3} instead of 0.37

292 μm^{3}cm^{-3}). Thus, presentation of cross section per a unit of volume σ_F^V appears more trustable.

293 We should recall also, that comparison of σ_F^V for different aerosol types makes sense only at low

294 RH, when the water uptake effect is small. The results in Table 2 are given for the heights, where

295 RH is below 20%. The fluorescence cross sections σ_F^V for November 30th and January 16th are

296 very close, but for the dust layer (February 6-7th, 2020), the cross section is about a factor 4

297 lower. From the data presented it is also possible to estimate the spectral differential cross

298 section, $\dfrac{\sigma_F^V}{\Delta\lambda}$, where $\Delta\lambda$ is the width of the filter transmission band.

299   It is rather difficult to validate our values of the fluorescence differential cross section. We

300 nevertheless compare them to in situ ground-based fluorescence measurements. Such reference

301 data are available mainly for biological particles (e.g. Pan, 2015). For biological particles, the

302 highest $\dfrac{d\sigma_F}{d\lambda}$ value, for a single particle with diameter 1.2 μm – 3.0 μm varies in the range (1-

303 100)*10^{-15} cm^{2}sr^{-1}nm^{-1} when stimulating radiation at 365 nm is used (Pan, 2015). Thus, our

304 estimated values look reasonable, keeping in mind that the fluorescence cross section of the

305 biological particles is higher than that of smoke. Still the results presented in the Table 2 should

306 be considered as qualitative and for obtaining quantitative values father studies are needed.

307

308   *3.2. Fluorescence of aerosol particles within cloud layers*

309   One of the attractive features of the fluorescence technique is the possibility to detect

310 aerosol and derive its content within the cloud layer. However the interpretation of fluorescence

311 measurements in the clouds is rather complicated. Aerosol can be inside the cloud droplets in

312 dissolved or solid state (activated CNN) or in the form of interstitial particles at 100% RH and

313   we need to separate somehow their contribution to the fluorescence signal. The fluorescence

314   backscattering β_F is calculated from the ratio of fluorescence and nitrogen Raman lidar signals

315   and it can be affected by the multiple scattering effects due to significant wavelength separation

316   between Raman and fluorescence components. Thus most trustable observations should be near

317   the cloud base.

318   The results of measurements in the presence of thin cloud layers on November 13th and

319   18th are shown in Fig. 4. The backscattering coefficients are given at 532 nm, because in the

320   cloud layers the detector in 1064 nm channel was sometimes saturated. On November 13th, the

321   cloud layers lead to a strong oscillation of β_{532} within 1000 m – 3000 m range. The spikes in β_{532}

322   profile, however, are not followed by synchronous increase of the fluorescence backscattering β_F

323   in the range of 1000—3000 m. On 18th November, the cloud layer within 1500 – 2000 m range

324   exhibit an even stronger elastic backscattering, exceeding 80 $Mm^{-1}sr^{-1}$, and again, no significant

325   change of fluorescence backscattering is observed. Thus observations in Fig.4 do not reveal

326   unambiguous effect of cloud layers on aerosol fluorescence Moreover, these results clearly

327   indicate the absence of leaks/contamination of elastic scattering in the fluorescence channel.

328   The situation, however, can be different, when the cloud droplets are formed on the aerosol

329   particles. Fig.5 shows the height – temporal distributions of the lidar signal at 1064 nm and the

330   fluorescence backscattering coefficient on the night 19-20th November 2019. After 21:50 UTC a

331   thin cloud layer starts to form at the top of the PBL resulting in simultaneous increase of β_F. To

332   quantify the influence of cloud water droplet on the fluorescence backscattering, Fig.6a provides

333   profiles of aerosol and fluorescence backscattering coefficients for two temporal intervals 20:00

334   – 21:30 UTC and 21:30 – 00:30 UTC, prior and after the cloud layer formation respectively.

335   Prior to cloud formation the aerosol load is very low, so backscattering is provided only at 1064

336   nm and to be distinguished at this figure, the value of β_{1064} is multiplied by factor 100. For 20:00

337   – 21:30 β_{1064} at 1500 m (height where the cloud forms) is about 0.07 $Mm^{-1}sr^{-1}$. Corresponding

338   value at 532 nm should be about 0.15 $Mm^{-1}sr^{-1}$ (for backscattering Angstrom exponent of 1.0).

339   After the cloud formation the backscattering coefficient is shown at 532 nm, because 1064 nm

340   detector in the cloud layer was overloaded. The β_{532} at 1500 m is of 500 $Mm^{-1}sr^{-1}$, thus β_{532}

341   increases by a factor of 3000 roughly, while β_F increases by approximately a factor 5.

342   Similar scenario occurred on the night 23-24th November 2019 (Fig.6b). Prior to the cloud

343   formation (21:00 – 23:00 UTC) the backscattering coefficient at 900 m height is β_{1064}=0.02 $Mm^{-1}sr^{-1}$

344   (β_{532} should be about 0.02 $Mm^{-1}sr^{-1}$) and after cloud formation β_{532} increases up to 130 $Mm^{-1}sr^{-1}$.

345   Thus β_{532} enhancement is of factor of 6500, while β_F again increases about factor 5. The

346   profiles of β_F in Fig.6 prior and after the cloud formation remain the same, below the cloud. It

347 corroborates the suggestion that the cloud was not transported by the air masses with different
348 properties, but the process of water vapor condensation occurs.

349   We should emphasize, that the enhancement of β_F can not be explained by just insufficient
350 suppression of elastic scattering. The enhancement was observed only inside an aerosol layer,
351 while clouds with similar backscattering coefficients, but outside the aerosol layer, didn't
352 provide the increase of β_{532}. As mentioned above, the fluorescence scattering phase function of
353 water microspheres can have a peak in the backward direction (Veselovskii et al., 2002a),
354 leading to increase of β_F, for a particle dissolved in a droplet, by approximately a factor 2
355 comparing to a solid particle. This is lower than the observed value, and at a moment we are not
356 capable to identify the mechanisms responsible for β_F enhancement. Just should be mentioned,
357 that in principle, water environment may affect the fluorescence efficiency. For example, the
358 fluorescence cross section of wet bacterial spores is higher than that of dry ones (Kunnil et al.,
359 2004). For insoluble particles the presence of a water shell can lead also to additional increase of
360 the fluorescence, due to the lens effect produced by the droplet. More studies are needed to
361 understand the influence of the water uptake by the particle during cloud formation on the
362 fluorescence backscattering.

363   One of the objectives of this study was to demonstrate the possibility to monitor aerosol
364 within a cloud by fluorescence. Fig.7 shows the height − temporal distributions of the range
365 corrected lidar signal at 1064 nm and the fluorescence backscattering β_F on November 15th 2019
366 for 2:45 − 6:15 UTC period. Low cloud layer appears at approximately 2000 m and a signal of
367 aerosol fluorescence is observed within this layer up to 3000 m. The HYSPLIT back trajectory
368 analysis shows that air masses at this height are transported over Atlantic from Canada. The
369 vertical profiles of β_{532} and β_F, integrated over 2:45 − 6:15 temporal interval, are shown in
370 Fig.8a. Fluorescence backscattering is about $0.03*10^{-4}$ $Mm^{-1}sr^{-1}$ at 1500 m and it rises to
371 $0.045*10^{-4}$ $Mm^{-1}sr^{-1}$ at 2000 m, near the cloud base, where RH can be close to 100%. Inside the
372 cloud β_F increases up to $0.07*10^{-4}$ $Mm^{-1}sr^{-1}$ at 3000 m, where elastic backscattering is maximal.
373 Thus total increase of β_F in 1500 − 3000 m range is slightly above a factor 2 and probably can be
374 attributed to the water uptake by the particles. High value of β_F in the cloud is probably due to
375 the contribution of interstitial aerosol particles.

376   On November 25th 2019 (Fig.8b), a low cloud layer at 850 m leads to increase of β_F by
377 approximately a factor 2, in a similar way as in Fig.6. However, above 1000 m the aerosol
378 content is very low and β_F is below $0.005*10^{-4}$ $Mm^{-1}sr^{-1}$. The sensitivity of the fluorescence
379 measurements can be limited by the fluorescence of the optics in the lidar receiver. The lowest
380 value of β_F observed in our measurements (averaged over several hundred meters height range)
381 was about $0.004*10^{-4}$ $Mm^{-1}sr^{-1}$, thus β_F in Fig.8b can be below the limit of our sensitivity. Above

382 2000 m strong cloud layer, with maximal value of β_{532} above 100 Mm^{-1}sr^{-1}, occurs. Back
383 trajectory analysis demonstrates that air masses at this height are transported over Atlantic from
384 the south of USA. The β_F in the cloud, averaged over 2200 – 2750 range, is about 0.006*10^{-4}
385 Mm^{-1}sr^{-1}, which is significantly lower than in Fig.8a. Thus on 25 November the cloud is less
386 "polluted" by aerosol than on 15 November. The fluorescence signal can be produced by both
387 activated CCN and by interstitial aerosol particle, and at a present stage we are not able to
388 separate their contributions.
389
390 **Conclusion**
391   In our research we analyzed the feasibility of the fluorescence channel, added to the
392 multiwavelength Mie-Raman lidar, for aerosol characterization. The results obtained,
393 demonstrate that the use of an interference filter for selection the part of the fluorescence
394 spectrum allows efficient lidar operation. In particular, LILAS lidar with the interference filter of
395 44 nm width in the fluorescence channel, was able to detect fluorescence signal from weak
396 aerosol layers ($\beta_{1064} <$ 0.02 Mm^{-1}sr^{-1}) up to 5000 m. During the experiment the fluorescence
397 capacity $G_F = \dfrac{\beta_F}{\beta_{1064}}$ of aerosol at condition of low RH varied through the (0.6 – 2.5)×10^{-4} range,
398 being the highest for the smoke and the lowest for the dust particles.
399   The lidar measurements, in principle, allow to get the information about the aerosol
400 fluorescence cross section in the elevated aerosol layers. For several atmospheric situations the
401 rough estimations of the fluorescence cross section were performed in this study and the results
402 obtained look reasonable, comparing with published values for biological particles. Still these
403 results should be taken as preliminary and the next important step in quantification of the
404 fluorescence measurements will be the system calibration, using a lamp with known spectrum.
405 As well, more deep comparison of σ_F obtained from the laboratory and lidar measurements, for
406 different aerosol types, is needed for validation. The fluorescence and multiwavelength Mie-
407 Raman lidar techniques are complimentary: the multiwavelength lidar allows aerosol typing and
408 estimation of the particle number and volume densities, that are later used to derive the
409 fluorescence cross sections from observed β_F. The fluorescence measurements, in turn, help to
410 improve the aerosol classification. The synergy of fluorescence and multi-wavelength lidar
411 techniques was not realized in this study, due to too low aerosol loading in November – February
412 period. However, we plan new experiments during Spring – Summer season, when AOD is
413 larger in Lille.

414   Results presented demonstrate also, that the fluorescence technique can be used to
415   monitor the aerosol particles inside the cloud (at least near the cloud base, if penetration depth of
416   the laser radiation is small), which is important in the study of aerosol – cloud interaction.
417   However to get quantitative information about particle properties we need deeper understanding
418   of influence of the water uptake by the particles on the fluorescence efficiency. In particular, in
419   the clouds formed at the top or inside the aerosol layer, an increase of the fluorescence
420   backscattering coefficient up to factor 5) was observed, and at a moment we are not able to
421   specify the processes behind this enhancement.

422   In coming studies we plan additional modifications of the lidar. In particular, we consider
423   the possibility to add second fluorescence channel near 550 nm, which should improve
424   selectivity of the fluorescence technique to different aerosol types. The water vapor channel will
425   be returned back to the system, which is essential for the study of particle hygroscopic growth.
426   Collocated measurements of the microwave radiometer of the Laboratoire d'optique
427   atmosphérique will be used to derive the RH profiles.

428

436

437

438 Table 1. Parameters of the biomass burning (BB), URban and DUst particles used in the model.

439 The volume $V^{N=1}$ and backscattering coefficient $\beta_{1064}^{N=1}$ are given for a single particle ($N=1$).

440

Type	$r_{V,f}$ μm	$r_{V,c}$ μm	σ_f	σ_c	$\dfrac{C_{V,f}}{C_{V,c}}$	CRI $_{1064}$	$V^{N=1}$ μm^3/cm^3	$\beta_{1064}^{N=1}$ Mm^{-1}sr^{-1}
BB	0.12	3.95	0.4	0.75	1.32	1.51-i.0.02	5.91E-3	1.58E-4
URban	0.175	3.275	0.38	0.75	2.5	1.4-i0.003	1.61E-2	4.69E-4
DUst	0.12	2.32	0.4	0.6	0.05	1.56- i0.001	7.6E-2	2.83E-3

441

442

443

444

445

446 Table.2. The aerosol parameters in elevated layers for three measurement sessions from Fig.3,

447 including the fluorescence β_F and aerosol β_{1064} backscattering coefficients, number N and volume

448 V particle densities, the differential fluorescence cross sections per a single particle $\dfrac{\sigma_F}{N}$ and per

449 unit volume $\dfrac{\sigma_F}{V}$, together with spectral density $\dfrac{\sigma_F}{V\Delta\lambda}$.

Date	Height km	β_F, Mm^{-1}sr^{-1}	β_{1064}, Mm^{-1}sr^{-1}	N, cm^{-3}	V, μm^{3}cm^{-3}	$\dfrac{\sigma_F}{N}$, 10^{-15} cm^{2}sr^{-1}	$\dfrac{\sigma_F}{V}$, 10^{-13} cm^{2}sr^{-1}μm^{-3}	$\dfrac{\sigma_F}{V\Delta\lambda}$, 10^{-15} cm^{2}sr^{-1}μm^{-3}nm^{-1}
30 Nov	4.0	3.0E-6	0.010	63	0.37	0.48	0.81	1.84
16 Jan	5.0	4.88E-6	0.013	82	0.60	0.48	0.81	1.84
6-7 Feb	2.9	5.63E-6	0.096	34	2.58	2.18	0.22	0.5

450

451

452

References

453

454   Alexandrov, M. and Mishchenko, M.: Information content of bistatic lidar observations of

455   aerosols from space, Opt. Expr. 25, 134-150, 2017.

456   Ansmann, A., Riebesell, M., Wandinger, U., Weitkamp, C., Voss, E., Lahmann, W., and

457   Michaelis, W.: Combined Raman elastic-backscatter lidar for vertical profiling of moisture,

458   aerosols extinction, backscatter, and lidar ratio, Appl.Phys.B*, 55*, 18-28, 1992.

459   Burris, J., McGee, T.J., Heaps, W.: UV Raman cross sections in nitrogen, Appl. Spectroscopy

460   46, 1076, 1992.

461   Burton, S. P., Ferrare, R. A., Hostetler, C. A., Hair, J. W., Rogers, R. R., Obland, M. D., Butler,

462   C. F., Cook, A. L., Harper, D. B., and Froyd, K. D.: Aerosol Classification of Airborne High

463   Spectral Resolution Lidar Measurements − Methodology and Examples, Atmos. Meas. Tech.,

464   5, 73–98, doi:10.5194/amt-5-73-2012, 2012.

465   Burton, S. P., Chemyakin, E., Liu, X., Knobelspiesse, K., Stamnes, S., Sawamura, P., Moore, R.

466   H., Hostetler, C. A., and Ferrare, R. A.: Information content and sensitivity of the 3β+2α

467   lidar measurement system for aerosol microphysical retrievals, Atmos.Meas. Tech., 9, 5555–

468   5574, 2016.

469   Dubovik, O., Holben, B., Eck, T.F., Smirnov, A., Kaufman, Y.J., King, M.D., Tanre, D.,

470   Slutsker, I.: Variability of absorption and optical properties of key aerosol types observed in

471   worldwide locations, J. Atmos. Sci., 59, 590–608, 2002.

472   Dubovik, O., Sinyuk, A., Lapyonok, T., Holben, B.N., Mishchenko, M., Yang, P., Eck, T.F.,

473   Volten, H., Munoz, O., Veihelmann, B., van der Zande, W.J., Leon, J.-F., Sorokin, M.,

474   Slutsker, I.: Application of spheroid models to account for aerosol particle nonsphericity in

475   remote sensing of desert dust, *J. Geophys. Res*., 111, D11208, doi:10.1029/2005JD006619,

476   2006.

477   Hill, S. C., Williamson, C. C., Doughty, D. C, Pan, Y.-L., Santarpia, J. L., Hill, H. H.: Size-

478   dependent fluorescence of bioaerosols: Mathematical model using fluorescing and absorbing

479   molecules in bacteria, J. Quant. Spectr. Radiat. Trans., 157, 54–70, 2015.

480   Horvath, H., Gunter, R. L., and Wilkison, S. W.: Determination of the coarse mode of the

481   atmospheric aerosol using data from a forward-scattering spectrometer probe, Aerosol

482   Sci. Technol., 12, 964–980, 1990.

483   Hu, Q., Goloub, P., Veselovskii, I., Bravo-Aranda, J.-A., Popovici, I., Podvin, T., Haeffelin, M.,

484   Lopatin, A. , Dubovik, O., Pietras, C., Huang, X., Torres, B., and Chen, C.: Long-range-

485   transported Canadian smoke plumes in the lower stratosphere over northern France, Atmos.

486   Chem. Phys. 19, 1173 – 1193, 2019. doi.org/10.5194/acp-19-1173-2019.

Huffman, J.A., Perring, A.E., Savage, N.J., Clot, B., Crouzy, B., Tummon, F., Shoshanim, O., Damit, B., Schneider, J., Sivaprakasam, V., Zawadowicz, M.A., Crawford, I., Gallagher, M., Topping, D., Doughty, D.C., Hill, S.C., Pan, Y.: Real-time sensing of bioaerosols: Review and current perspectives, Aerosol Science and Technology, 2019. DOI: 10.1080/02786826.2019.1664724

Immler, F., Engelbart, D., Schrems, O.: Fluorescence from atmospheric aerosol detected by a lidar indicates biogenic particles in the lower stratosphere, Atmos. Chem. Phys. 5, 345–355, 2005.

Kerker, M., and Druger, S. D.: Raman and fluorescent scattering by molecules embedded in spheres with radii up to several multiples of the wavelength, Appl. Opt. 18, 1172–1179, 1979.

Klett J.D., "Lidar inversion with variable backscatter/extinction ratios", Appl.Opt. 24, 1638-1643, 1985.

Kunnil, J., Swartz, B., Reinisch, L.: Changes in the luminescence between dried and wet bacillus spores, Appl. Opt. 43, 5404 – 5409, 2004.

Li, B., Chen, S., Zhang, Y., Chen, H., Guo, P.: Fluorescent aerosol observation in the lower atmosphere with an integrated fluorescence-Mie lidar, J. Quant. Spectr. Rad. Transf., 227, 211–218, 2019.

Luís Guerrero-Rascado, J., Amiridis, V., Kokkalis, P., Apituley, A., Baars, H., Schwarz, A., Wandinger, U., Binietoglou, I., 660 Nicolae, D., Bortoli, D., Comerón, A., Rodríguez-Gómez, A., Sicard, M., Papayannis, A. and Wiegner, M.: An automatic observation-based aerosol typing method for EARLINET, Atmos. Chem. Phys., 18, 15879–15901, doi:10.5194/acp-18-15879-2018, 2018.

Miyakawa, T., Kanaya, Y., Taketani, F., Tabaru, M., Sugimoto, N., Ozawa, Y., and Takegawa, N.: Ground-based measurement of fluorescent aerosol particles in Tokyo in the spring of 2013: potential impacts of nonbiological materials on autofluorescence measurements of airborne particles, J. Geophys. Res. Atmos., 120, 1171–1185, 2015, doi:10.1002/2014JD022189.

Müller, D., Wandinger, U., and Ansmann, A.: Microphysical particle parameters from extinction and backscatter lidar data by inversion with regularization: theory, Appl. Opt. 38, 2346-2357, 1999.

Pan, Y.L., Hill, S.C., Wolf, J.P., Holler, S., Chang, R.K., Bottiger, J.R.: Backward-enhanced fluorescence from clusters of microspheres and particles of tryptophan, Appl. Opt. 41, 2994-2999, 2002.

521 Pan, Y.-L., Pinnick, R.G., Hill, S.C., Rosen, J.M., and Chang, R.K.: Single-particle laser-
522   induced-fluorescence spectra of biological and other organic-carbon aerosols in the
523   atmosphere: Measurements at New Haven, Connecticut, and Las Cruces, New Mexico, J.
524   Geophys. Res., 112, D24S19, doi:10.1029/2007JD008741, 2007.

525 Pan, Y.-L.: Detection and characterization of biological and other organic-carbon aerosol
526   particles in atmosphere using fluorescence, J. Quant. Spectr. Radiat. Trans. 150, 12–35, 2015

527 Rao, Z., He, T., Hua D, Wang, Y., Wang, X., Chen, Y., Le J.: Preliminary measurements of
528   fluorescent aerosol number concentrations using a laser-induced fluorescence lidar, Appl.
529   Opt. 57, 7211-7215, 2018.

530 Reichardt, J.: Cloud and aerosol spectroscopy with Raman lidar, J. Atm. Ocean. Tech., 31,
531   1946-1963, 2014.

532 Reichardt, J., Leinweber, R., Schwebe, A.: Fluorescing aerosols and clouds: investigations of co-
533   existence, Proceedings of the 28th ILRC, Bucharest, Romania, 25-30 June, 2017.

534 Saito, Y., Ichihara, K., Morishita, K., Uchiyama, K., Kobayashi, F., Tomida, T.: Remote
535   detection of the fluorescence spectrum of natural pollens floating in the atmosphere using a
536   laser-induced-fluorescence spectrum (LIFS) lidar, Remote Sens., 10, 1533, 2018.
537   doi:10.3390/rs10101533.

538 Schnaiter, M., Linke, C., Mohler, O., Naumann, K. H., Saathoff, H., Wagner, R., Schurath, U.,
539   and Wehner, B.: Absorption amplification of black carbon internally mixed with secondary
540   organic aerosol, J. Geophys. Res., 110, D19204, 2005.

541 Stein, A.F., Draxler, R.R, Rolph, G.D., Stunder, B.J.B., Cohen, M.D., and Ngan, F.: NOAA's
542   HYSPLIT atmospheric transport and dispersion modeling system, Bull. Amer. Meteor. Soc.,
543   96, 2059-2077, 2015. http://dx.doi.org/10.1175/BAMS-D-14-00110.1

544 Sugimoto, N., Huang, Z., Nishizawa, T., Matsui, I., Tatarov, B.: Fluorescence from atmospheric
545   aerosols observed with a multichannel lidar spectrometer," Opt. Expr. 20, 20800-20807,
546   2012.

547 Tesche, M., Groß, S., Ansmann, A., Müller, D., Althausen, D., Freudenthaler, V., and Esselborn,
548   M.: Profiling of Saharan dust and biomass-burning smoke with multiwavelength polarization
549   Raman lidar at Cape Verde, Tellus B, 63, 649–676, doi:10.1111/j.1600-0889.2011.00548.x,
550   2011.

551 Venable, D. D., Whiteman, D. N., Calhoun, M. N., Dirisu, A.O., Connell, R. M., Landulfo, E.:
552   Lamp mapping technique for independent determination of the water vapor mixing ratio
553   calibration factor for a Raman lidar system, Appl. Opt., 50, 4622 - 4632, 2011.

554 Veselovskii, I., Griaznov, V., Kolgotin, A., Whiteman, D.: "Angle- and size-dependent
555   characteristics of incoherent Raman and fluorescent scattering by microsoheres 2.: Numerical
556   simulation", Appl. Opt. 41, 5783-5791, 2002a.

557 Veselovskii I., Kolgotin, A., Griaznov, V., Müller, D., Wandinger, U., Whiteman, D.: Inversion
558   with regularization for the retrieval of tropospheric aerosol parameters from multi-
559   wavelength lidar sounding, Appl.Opt. 41, 3685-3699, 2002b.

560 Veselovskii, I., Goloub, P., Hu, Q., Podvin, T., Whiteman, D. N., Korenskiy, M., Landulfo, E.:
561   Profiling of CH4 background mixing ratio in the lower troposphere with Raman lidar: a
562   feasibility experiment., Atmos. Meas. Tech. 12, 119–128, 2019. doi.org/10.5194/amt-12-
563   119-2019.

564 Veselovskii, I., Hu, Q., Goloub, P., Podvin, T., Korenskiy, M., Derimian, E., Legrand, M.,
565   Castellanos, P.: Variability of Lidar-Derived Particle Properties Over West Africa Due to
566   Changes in Absorption: Towards an Understanding. Atm. Chem. Phys., 20, 6563-6581,
567   2020.

568 Whiteman, D. N., B. Demoz, P. Di Girolamo, J. Comer, I. Veselovskii, K. Evans, Z. Wang, M.
569   Cadirola, K. Rush, G. Schwemmer, B. Gentry, S. H. Melfi, B. Mielke, D. Venable, T. Van
570   Hove, "Raman Water Vapor Lidar Measurements During the International H2O Project. I.
571   Instrumentation and Analysis Techniques", J. Atmos. Oceanic Technol., 23, 157-169, 2006.
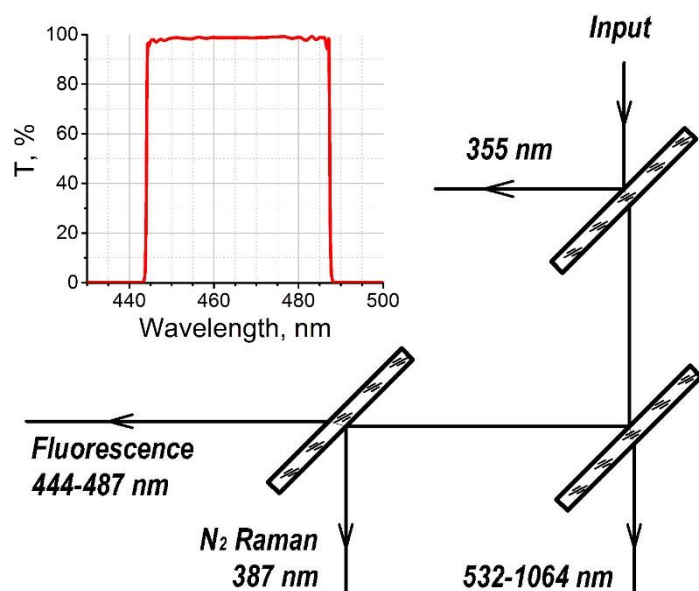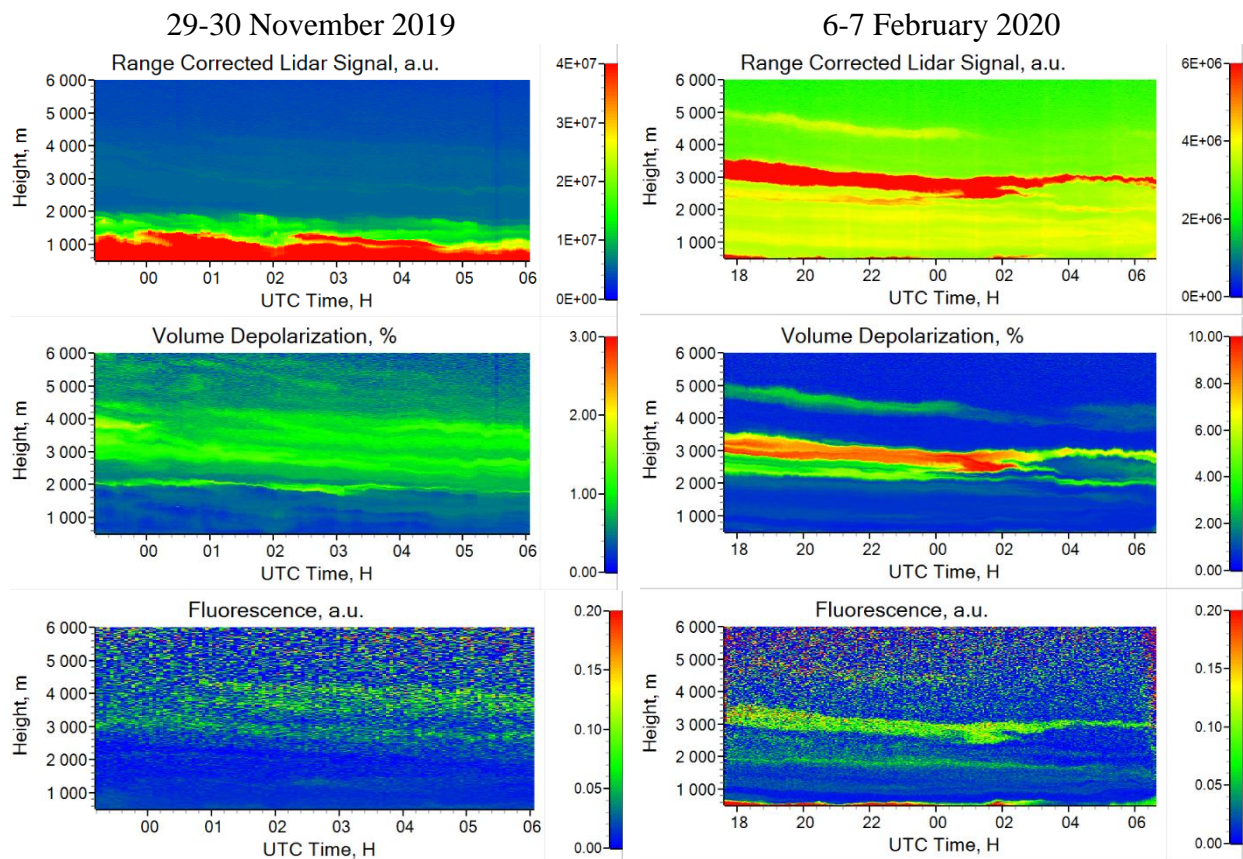
572

573 **Figures**

574

575

576

577

578

579 Fig.1 Optical scheme of the elastic, Raman and fluorescence backscatters separation together
580 with transmission curve of the interference filter in the fluorescence channel.

581

582

583

584

585

586

587

29-30 November 2019

6-7 February 2020

588 Fig.2. The range corrected lidar signal at 1064 nm, volume depolarization ratio δ_{1064} and
589 fluorescence backscattering measured at Lille, on 29-30 November 2019 (on the left) and 6-7
590 February 2020 (on the right).

591

592

21

593
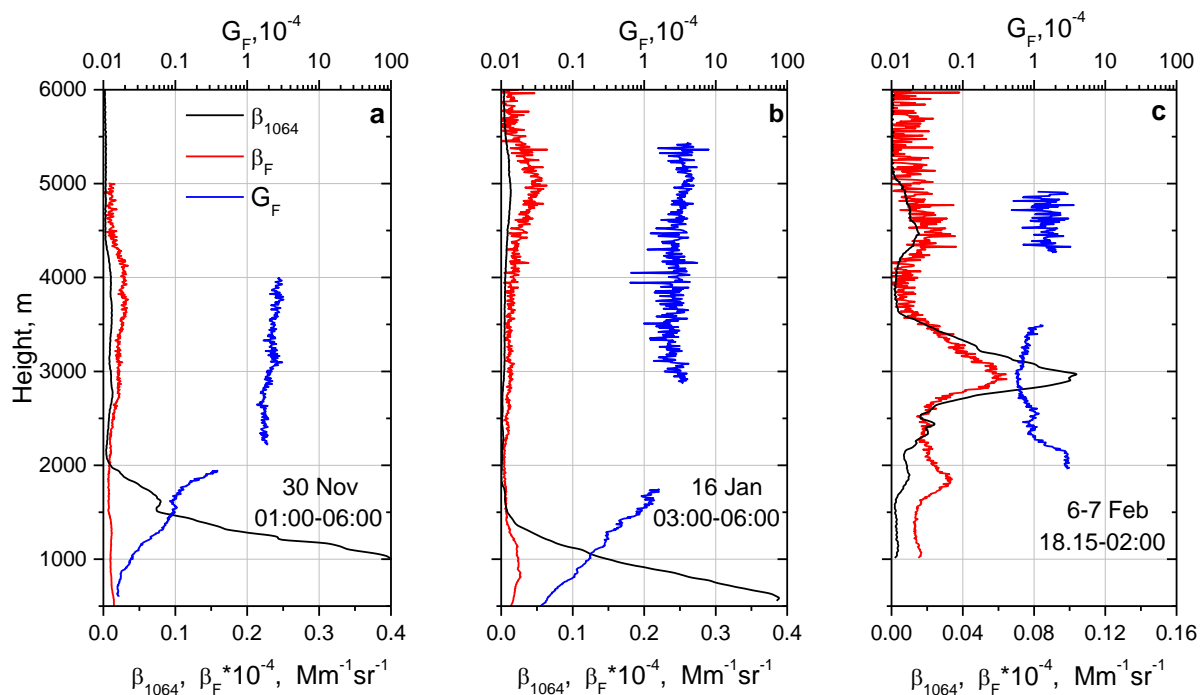
Fig.3 Vertical profiles of aerosol (β_{1064}) and fluorescence (β_F) backscattering coefficients together with the fluorescence capacity (G_F) on (a) 30 November 2019, (b) 16 January 2020 and (c) 6-7 February 2020.

594
595
596
597
598
599
600
601
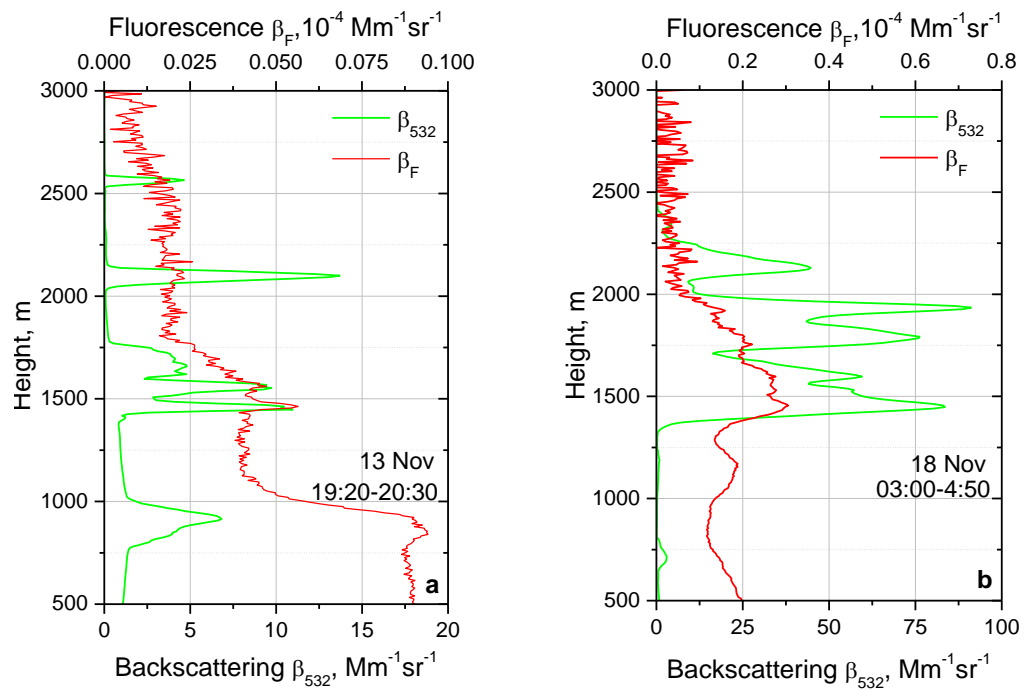
Fig.4. Aerosol (β_{532}) and fluorescence (β_F) backscattering coefficients on 13 and 18 November 2019.

607

608
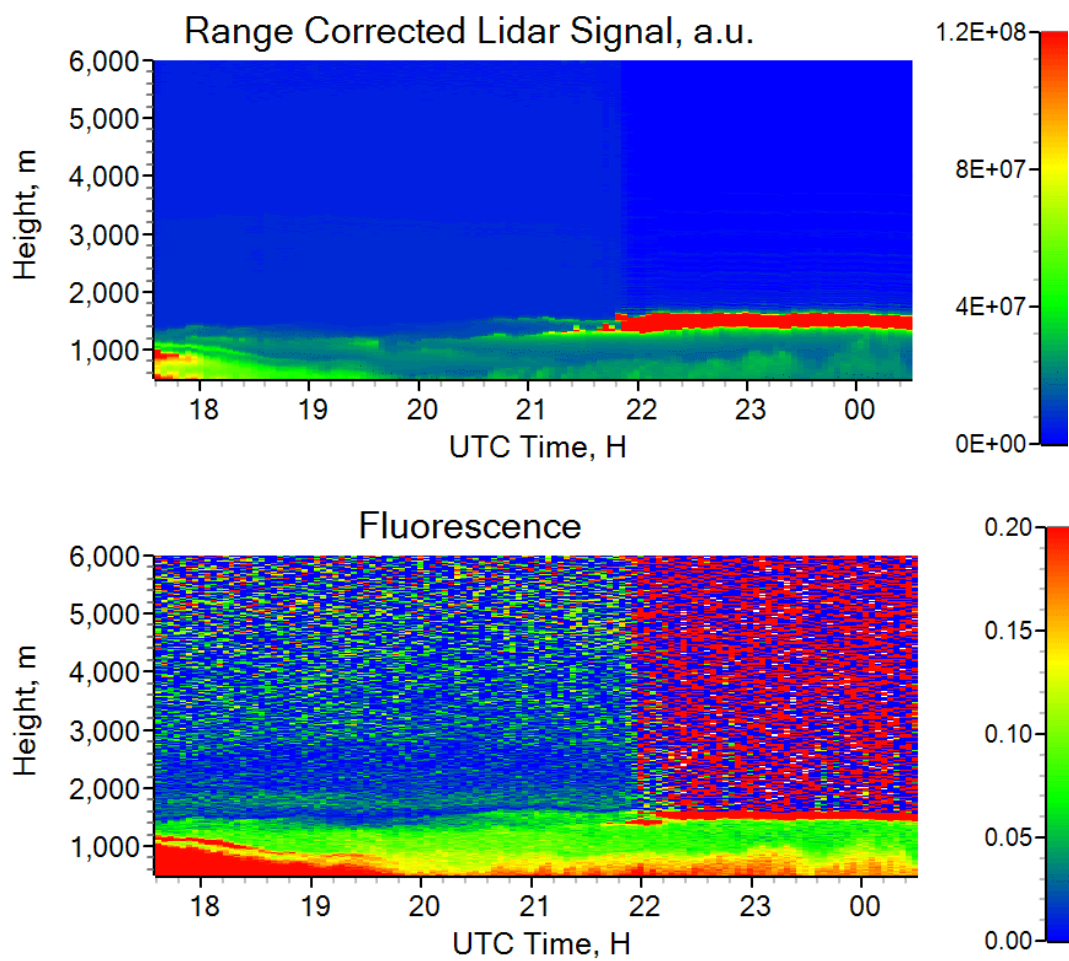
609

610

611

612   Fig.5. Height-temporal distribution of the range corrected lidar signal at 1064 nm and
613   fluorescence backscattering coefficient β_F (in arbitrary units) on 19-20 November 2019.
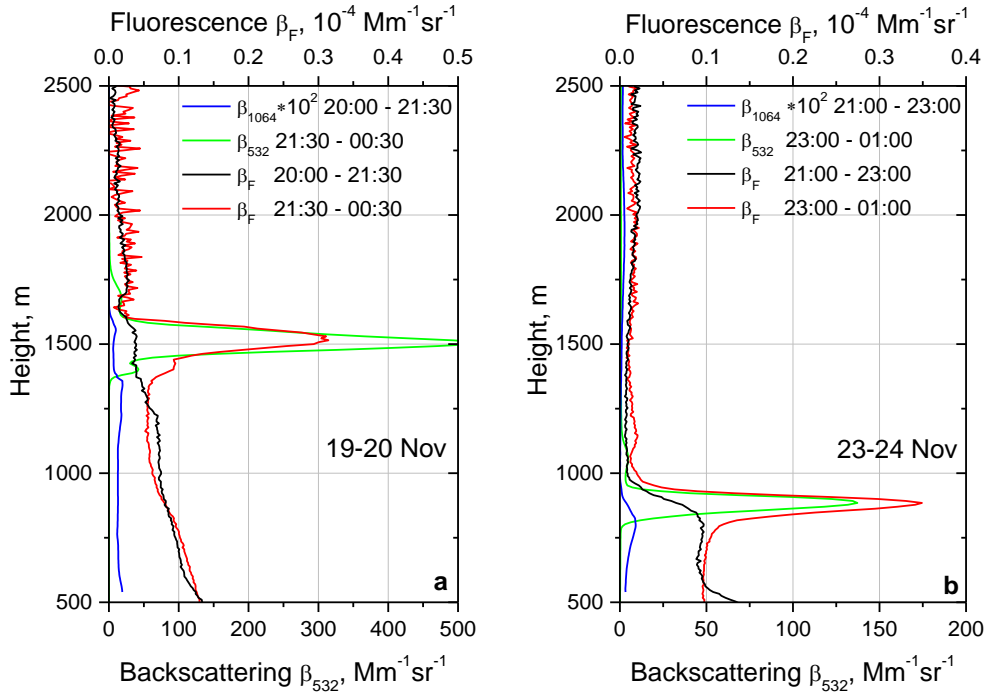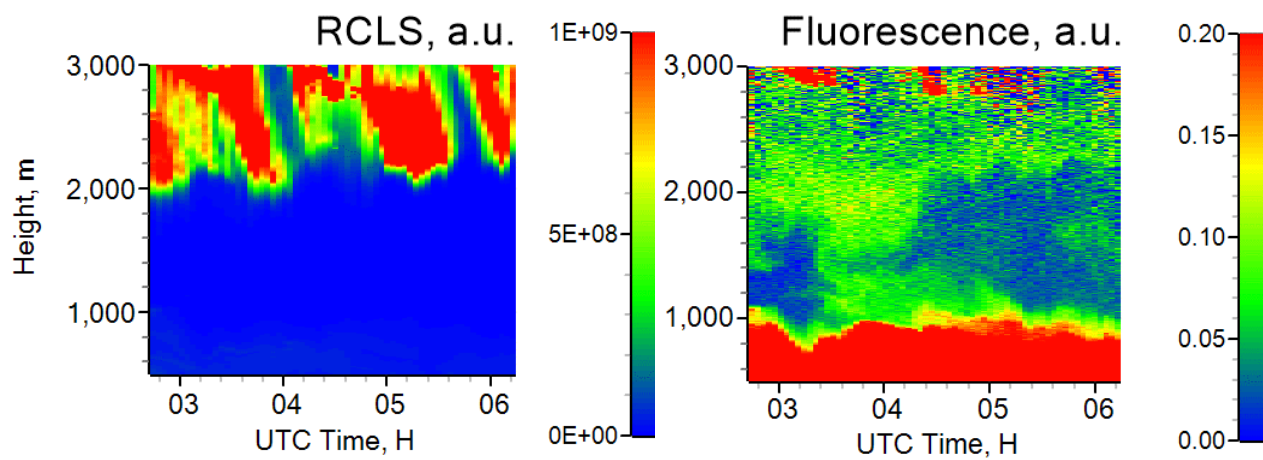
614　Fig.6. Aerosol and fluorescence backscattering coefficients on (a) 19-20 and (b) 23-24
615　November 2019 for two time intervals: prior and after cloud formation. Backscattering
616　coefficient β_{1064} prior to cloud formation is low, so it is multiplied by factor 100 to be
617　distinguished at this figure.

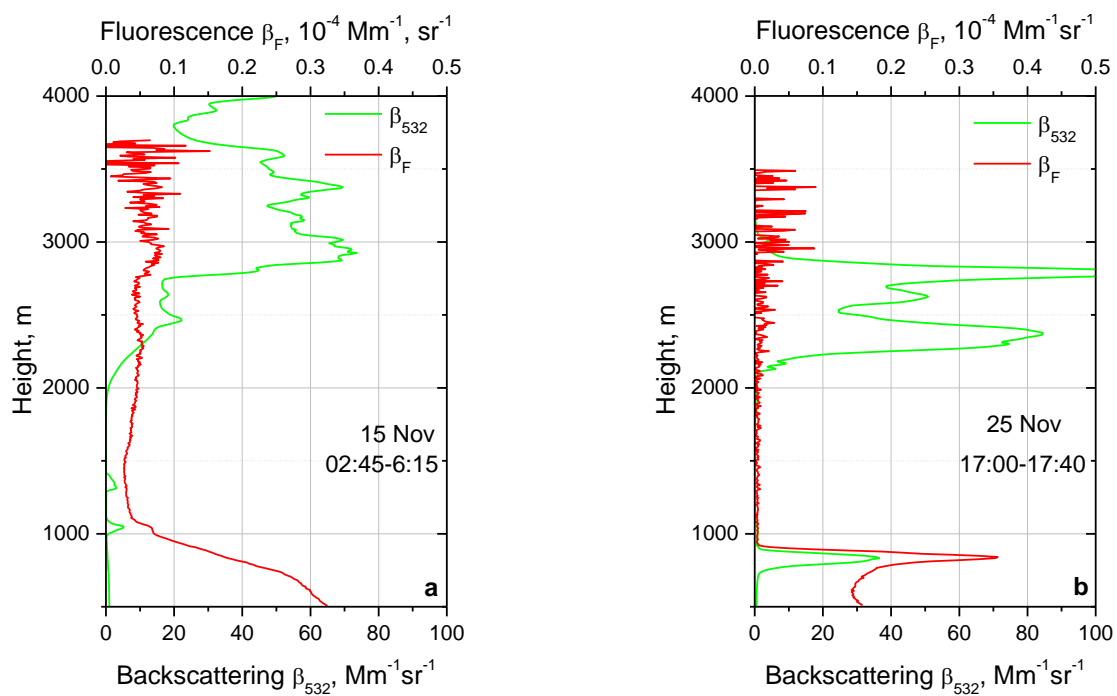618

619

620

621

622

623

624   Fig.7. Height-temporal distribution of the range corrected lidar signal (RCLS) at 1064 nm and

625   the fluorescence backscattering coefficient on 15 November 2019.

626

627

628   Fig.8. Aerosol (β_{532}) and fluorescence (β_F) backscattering coefficients on (a) 15 and (b) 25
629   November 2019.

630